Plasmon–phonon coupling in graphene–hyperbolic bilayer heterostructures*

Ge Yin(尹格), Jun Yuan(元军), Wei Jiang(姜玮), Jianfei Zhu(朱剑飞), and Yungui Ma(马云贵)†

State Key Laboratory of Modern Optical Instrumentation, Center for Optical and Electromagnetic Research, College of Optical Science and Engineering, Zhejiang University, Hangzhou 310058, *China*

(Received 8 April 2016; revised manuscript received 3 June 2016; published online 30 September 2016)

Polar dielectrics are important optical materials enabling the subwavelength manipulation of light in infrared due to their capability to excite phonon polaritons. In practice, it is highly desired to actively modify these hyperbolic phonon polaritons (HPPs) to optimize or tune the response of the device. In this work, we investigate the plasmonic material, a monolayer graphene, and study its hybrid structure with three kinds of hyperbolic thin films grown on SiO_2 substrate. The inter-mode hybridization and their tunability have been thoroughly clarified from both the band dispersions and the mode patterns numerically calculated through a transfer matrix method. Our results show that these hybrid multilayer structures are of strong potentials for applications in plasmonic waveguides, modulators and detectors in infrared.

Keywords: hyperbolic material, phonon polaritons, graphene, surface plasmons

PACS: 42.82.Fv, 42.70.Qs **DOI:** 10.1088/1674-1056/25/11/114216

1. Introduction

Polar dielectric crystals can show hyperbolic dispersion characters in infrared arising from their ionic resonance driven by external electromagnetic (EM) fields, such as having anisotropic dielectric constants with sign difference.[1] On their surfaces with air, bounded phonon polaritons could be excited in the resonance state. Like hyperbolic metamaterials, light with large wavevectors or high energy density state can propagate inside these kinds of natural indefinite anisotropic materials.[2,3] Many interesting phenomena and related technological applications can be inspired by these special materials as subwavelength imaging,[4] sensing engineering,[5] or enhanced light radiation.[6] However, like plasmonic behaviors of noble metals in the visible regime,[7,8] it is hard to actively control or modify the EM properties of a hyperbolic dielectric once the device is fabricated. In practice, activity or tunable function is often desired in order to optimize or modulate the device performance, particularly when considering the narrow band phonon resonance nature of polar dielectrics. For this aim conductive materials with variable charge densities through optical pumping or electric doping have been adopted in the design of reconfigurable plasmonic devices.[9] Among them, graphene due to the relatively low damping loss and wideband response has attracted great attention as a key variable component, especially in the heterostructures of graphene–hexagonal boron nitride (hBN) composite in recent years.[10,11] Electron oscillations in graphene and ionic vibrations in polar dielectrics can produce plasmon–phonon hybrid modes. This hybrid structure, regarded as an advanced version of two-dimensional (2D) metamaterials, can absorb the virtues of both the hyperbolic dielectric and graphene by offering more freedoms to manipulate infrared waves and thus create new functional optical devices.[12–14] It has been pointed out that graphene on a plasmonic dielectric substrate will possess larger carrier mobility than on a normal insulator such as SiO_2.[15] In principle, reconfigurable plasmonic devices or functionalities in infrared can be anticipated applying this hybrid structure plus the additional features of low-loss and wideband.

In this work, we systematically investigated three kinds of graphene–hyperbolic heterostructures including graphene–hBN, graphene–aluminum nitride (AlN) and graphene–zinc oxide (ZnO), which all show strong electron–phonon coupling resonance in the mid-infrared regime. Among these hyperbolic components, hBN has attracted most attentions due to the low loss and high field confinement that are promising for subwavelength device applications.[16] Here, we give more comprehensive discussions on the field patterns and their propagation features associated with the hybrid coupling with graphene, especially when the properties of graphene are varied. For AlN and ZnO their semi-conductor and optoelectronics properties have been widely investigated in the field of material science,[17,18] while their EM characteristics on surface plasmon polartitons (SPPs), in particular hybridizing with another plasmonic layer are less discussed. It is scientifically and also practically instrumental to explore their optical features as potential plasmonic material candidates for novel photonic phenomena or functionalities.

For graphene–hBN heterostructure, we examine the hy-

*Project supported by the National Natural Science Foundation of China (Grant No. 61271085) and the Natural Science Foundation of Zhejiang Province, China (Grant No. LR15F050001).

†Corresponding author. E-mail: yungui@zju.edu.cn

© 2016 Chinese Physical Society and IOP Publishing Ltd

brid polaritions in two different hyperbolic regions (Reststrahlen bands) and show that the propagation characteristics could be tuned by controlling the Fermi level. These two hyperbolic regions correspond to very different localized mode patterns. For the hybrid structure with AlN or ZnO constituent, which only has one hyperbolic resonance spectrum, our calculation shows that highly confined hybrid phonon–plasmonic modes could be achieved with proper damping parameters. Considering their optoelectronic properties, in particular for ZnO, more versatile or controlling features may be expected in a graphene–semiconductor hybrid system. Since the electric properties of the graphene layer can be vividly modified e.g., by applying a gate voltage[19] or optical pumping,[20] the hybrid plasmonic properties in principle could be tuned in both amplitude and wavelength. Hyperbolic responses of the polar crystals are usually narrow band and the hybrid combinations of different constituents proposed here may afford the options to realize the desired functionality in different spectrum regimes.

2. Theoretical model

The multilayer hybrid topology investigated here is air/graphene/hyperbolic material (hBN, AlN, ZnO) /SiO_2 substrate. The graphene layer we used is a monolayer sheet and treated as a 2D infinite material. The structure is infinite in the xy plane (Fig. 1) with the illumination of a p polarized plane wave. In Fig. 1, the middle grey region ($-d < z < 0$) represents the hyperbolic layer and the top (bottom) region is air (SiO_2 substrate). Here we employ the standard transfer matrix method[21] to derive the reflection coefficient r of the hybrid structures. For our 2D structures the magnetic field along the y-axis direction can be expressed as

$$H_i = [a_i \exp(\mathrm{i}k_i^z z_i) + b_i \exp(-\mathrm{i}k_i^z z_i)] \exp(\mathrm{i}k_i^x x), \quad (1)$$

where the variable $i = 1, 2, 3$ stands for the region of air, hyperbolic layer, and SiO_2, respectively. k_i^z and k_i^x are the wavevector components along the z and x axes, respectively. They satisfy the dispersion relation $k_i^{z^2}/\varepsilon_i^x + k_i^{x^2}/\varepsilon_i^z = \omega^2/c^2$, where ε_i^x and ε_i^z are dielectric permittivity along the x and z axes, respectively. a_i and b_i are the coefficients of the incident and reflected waves, respectively. From the boundary continuity condition, we have the in-plane wavevector $k_1^x = k_2^x = k_3^x = k^x$.

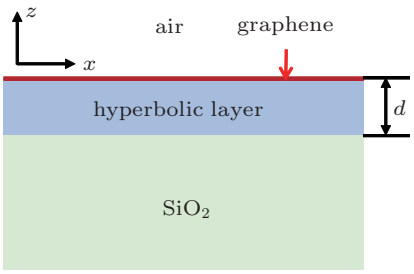


Fig. 1. (color online) Schematic of the hybrid structure in our calculation. The graphene monolayer (red) is sandwiched by top air and bottom hyperbolic layer (thickness d) grown on the SiO_2 substrate. This two-dimensional composite structure is infinity along the y-axis direction.

The coefficients of the wave components in different regions are connected by a matrix equation

$$\begin{pmatrix} a_1 \\ b_1 \end{pmatrix} = \boldsymbol{M} \begin{pmatrix} a_3 \\ b_3 \end{pmatrix}, \quad (2)$$

where the transfer matrix $\boldsymbol{M}$ is the product of three parts

$$\boldsymbol{M} = \boldsymbol{M}_{12}\boldsymbol{P}_{12}\boldsymbol{M}_{23}. \quad (3)$$

In Eq. (3), $\boldsymbol{M}_{12}$ ($\boldsymbol{M}_{23}$) represents the interface transfer matrix between regions 1 and 2 (regions 2 and 3) and $\boldsymbol{P}_{12}$ represents the propagation matrix in region 2, i.e., the hyperbolic layer. These matrices can be deduced by Maxwell's equations and boundary continuity conditions, defined by[21,22]

$$\boldsymbol{M}_{12} = \frac{1}{2\varepsilon_2^x k_1^z} \begin{pmatrix} \varepsilon_2^x k_1^z + \varepsilon_1^x k_2^z + \sigma \dfrac{k_2^z k_1^z}{\varepsilon_0 \omega} & \varepsilon_2^x k_1^z - \varepsilon_1^x k_2^z - \sigma \dfrac{k_2^z k_1^z}{\varepsilon_0 \omega} \\ \varepsilon_2^x k_1^z - \varepsilon_1^x k_2^z + \sigma \dfrac{k_2^z k_1^z}{\varepsilon_0 \omega} & \varepsilon_2^x k_1^z + \varepsilon_1^x k_2^z - \sigma \dfrac{k_2^z k_1^z}{\varepsilon_0 \omega} \end{pmatrix}, \quad (4)$$

$$\boldsymbol{M}_{23} = \frac{1}{2\varepsilon_3^x k_2^z} \begin{pmatrix} \varepsilon_3^x k_2^z + \varepsilon_2^x k_3^z & \varepsilon_3^x k_2^z - \varepsilon_2^x k_3^z \\ \varepsilon_3^x k_2^z - \varepsilon_2^x k_3^z & \varepsilon_3^x k_2^z + \varepsilon_2^x k_3^z \end{pmatrix}, \quad (5)$$

$$\boldsymbol{P}_{12} = \begin{pmatrix} \mathrm{e}^{-\mathrm{i}k_2^z d} & 0 \\ 0 & \mathrm{e}^{\mathrm{i}k_2^z d} \end{pmatrix}, \quad (6)$$

where d is the thickness of the hyperbolic layer, ε_0 is vacuum permittivity, σ is the conductivity of graphene, and ω is angular frequency.

According to Eq. (2), we can calculate the reflection coefficient $r = b_1/a_1$. The eigenmode in a non-dissipative system will be excited for a vanishingly small incident wave ($a_1 \approx 0$). In this case the poles of r at real k_x and ω give rise to the dispersion curve of the heterostructure.[16]

The conductivity σ of monolayer graphene in the infrared range is modeled using the local random phase approximation (RPA) expressed by[23,24]

$$\sigma_{\mathrm{intra}} = \frac{\mathrm{i}e^2 k_{\mathrm{B}} T}{\pi\hbar^2(\omega + \mathrm{i}\tau_{\mathrm{g}}^{-1})} \left(\frac{E_{\mathrm{F}}}{k_{\mathrm{B}}T} + 2\ln(\mathrm{e}^{-E_{\mathrm{F}}/k_{\mathrm{B}}T} + 1) \right),$$

$$\sigma_{\mathrm{inter}} = -\frac{\mathrm{i}e^2}{4\pi\hbar} \ln \left| \frac{2E_{\mathrm{F}} - (\omega + \mathrm{i}\tau_{\mathrm{g}}^{-1})\hbar}{2E_{\mathrm{F}} + (\omega + \mathrm{i}\tau_{\mathrm{g}}^{-1})\hbar} \right|,$$

$$\sigma = \sigma_{\text{inter}} + \sigma_{\text{intra}}, \tag{7}$$

where e is electron charge, $\hbar$ is reduced Planck constant, k_{B} is Boltzmann constant, T is temperature, E_{F} is the Fermi energy of graphene sheet, and τ_{g} is the electron relaxation time. The total conductivity σ is contributed by both interband (σ_{inter}) and intraband (σ_{intra}) conductions. The Fermi level of graphene layer can be tuned by many methods,[25] among which the most straightforward way is to apply a gate voltage. The electron relaxation time τ_{g} as a function of carrier mobility μ, Fermi energy E_{F}, and Fermi velocity V_{F} is written by $\tau_{\text{g}} = \mu E_{\text{F}}/(eV_{\text{F}}^2)$. In calculation we use $V_{\text{F}} = 10^6$ m/s and $\mu = 1000$ cm$^2\cdot$V$^{-1}\cdot$s^{-1} for a low-doping graphene. Accordingly, $E_{\text{F}} = 0.5$ eV and $\tau_{\text{g}} = 100$ fs, which are used in the literature.[26] The dielectric properties of the SiO_2 substrate are taken from Ref. [27]. According to these parameters the SiO_2 substrate will also contribute a phonon resonance near 1130 cm^{-1}, but which is neglected in our consideration due to its weak amplitude compared with the hyperbolic components of interest.

3. Results and discussion

3.1. With the hBN hyperbolic layer

Here the hyperbolic layer is assumed to be single crystal and the uniaxial direction is aligned parallel to the z-axis (Fig. 1). For hBN, the in-plane and out-of-plane dielectric functions can be described by the Lorentz model[28]

$$\varepsilon_{h,\perp(\parallel)} = \varepsilon_{\infty,\perp(\parallel)} + \varepsilon_{\infty,\perp(\parallel)} \frac{\omega_{\text{LO},\perp(\parallel)}^2 - \omega_{\text{TO},\perp(\parallel)}^2}{\omega_{\text{TO},\perp(\parallel)} - \omega^2 - \text{i}\omega\gamma_{\perp(\parallel)}}, \tag{8}$$

where $\perp(\parallel)$ represents the direction perpendicular (parallel) to the c-axis (or the z-axis in Fig. 1) of the optical crystal. The EM material parameters used in our calculation are given in Table 1. The calculated dispersions for hBN crystals are plotted in Fig. 2(a). As a typical Vander Waals crystal, hBN's phonon resonances are anisotropic and have different eigenfrequencies for the in-plane and out-of-plane oscillations. As a consequence, it has two hyperbolic regions shown in Fig. 2(a), the type-I region with $\text{Re}(\varepsilon_\perp) > 0$ and $\text{Re}(\varepsilon_\parallel) < 0$ in 780–830 cm^{-1} (shaded green) and the type-II region with $\text{Re}(\varepsilon_\perp) < 0$ and $\text{Re}(\varepsilon_\parallel) > 0$ in 1370–1610 cm^{-1} (shaded orange). The real part of permittivity changes the sign in these two regions. In Fig. 2(b), we plot the hyperbolic isofrequency curves for these two bands at 800 cm^{-1} (left) and 1500 cm^{-1} (right), respectively. These straight dispersion features at high wavevectors corresponding to uniform group velocity vectors are very important for subwavelength lensing applications.[29] It is seen that at 800 cm^{-1} group and phase velocities of light traveling in hBN will propagate in the opposite directions, i.e., behaving as the back-forward wave.

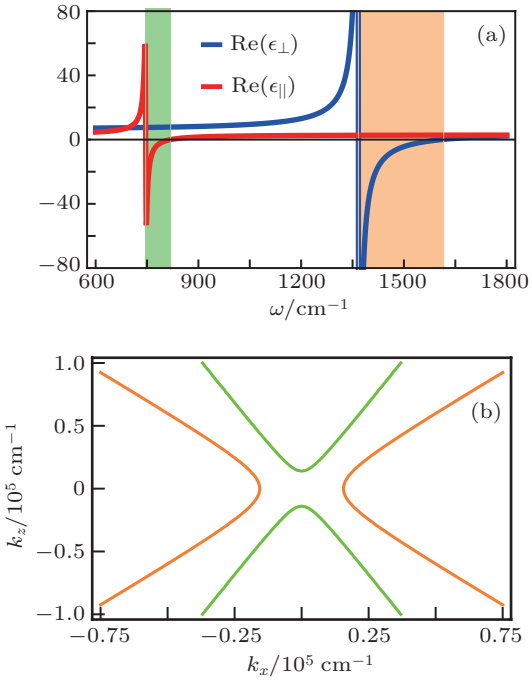


Fig. 2. (color online) Relative permittivity spectra (a) and isofrequency band dispersion (b) of hBN. The two shaded areas in panel (a) indicate the type I (green) and type II (orange) hyperbolic regions of hBN. Curves in panel (b) plot the corresponding isofrequency curves in these two regions at 800 cm^{-1} (green) and 1500 cm^{-1} (orange), respectively.

Table 1. Material parameters used in our calculation. Here ε_∞ is the high frequency dielectric constant. ω_{LO} and ω_{TO} are the longitudinal-optic (LO) and transverse-optic (TO) phonon resonance frequencies, respectively. γ_{LO} and γ_{TO} are the damping constants of LO and TO phonon resonances, respectively. These parameters are obtained from the previous publications.[16,30,31]

		ε_∞	ω_{LO}/cm^{-1}	ω_{TO}/cm^{-1}	γ_{LO}/cm^{-1}	γ_{TO}/cm^{-1}
hBN	$\perp$	4.87	1610	1370	5	–
	$\parallel$	2.95	830	780	4	–
AlN	$\perp$	4.53	912	670	6	9
	$\parallel$	4.72	890	610	8	11
ZnO	$\perp$	3.7	589	409	3	3
	$\parallel$	3.78	575	384	3	3

For the hybrid structure, we consider a 100-nm-thick hBN thin film as the hyperbolic layer. The resonant surface modes can be determined by the poles of the reflection coefficients and the mode dispersion patterns of the hybrid structure are obtained by plotting the imaginary part of the reflection coefficient r.[27,32] The results are given in Fig. 3 for the type-I region and in Fig. 4 for the type-II region. To better understand the mode characters, we also plot the field profiles of the modes at some frequency points as labeled in the dispersion patterns by dots. Figure 3(a) shows a monotonously increasing band curve for a free-standing graphene monolayer. The bounded mode pattern at 1700 cm^{-1} is plotted in Fig. 3(b) exhibiting a spatially symmetrical field distribution.

Figure 3(c) gives the dispersion diagram of the hBN film corresponding to the type-I band. Two distinct features are observed: (i) the Poynting vector S and the in-plane wavevector k_x point towards opposite directions, which means that in this

band the waves have negative phase velocity;[33] (ii) the first waveguide mode (node) has an integer index $m = 1$ which corresponds to an asymmetrical field distribution, for example as shown in Fig. 3(d). These two results are closely correlated to the hyperbolic dispersion features of the hBN constituent (see the green curve in Fig. 2(b)). More specifically, the minimum available value for the k_z component of the hBN film determines the lowest order number of the waveguide modes. For the type-I band, it has a cutoff wavenumber starting from ω/c, while it has no such a limit for the type-II band. Thus, as shown in Figs. 4(a) and 4(d), the first waveguide mode for the type-II band has an integer index $m = 0$. Different index number m corresponds to different mode pattern, following the characteristic equation $\delta_1 + \delta_2 + 2k_2^z d = 2m\pi$, where δ_1 and δ_2 are the reflection phase shifts of the top and bottom interface of the hyperbolic film, respectively.

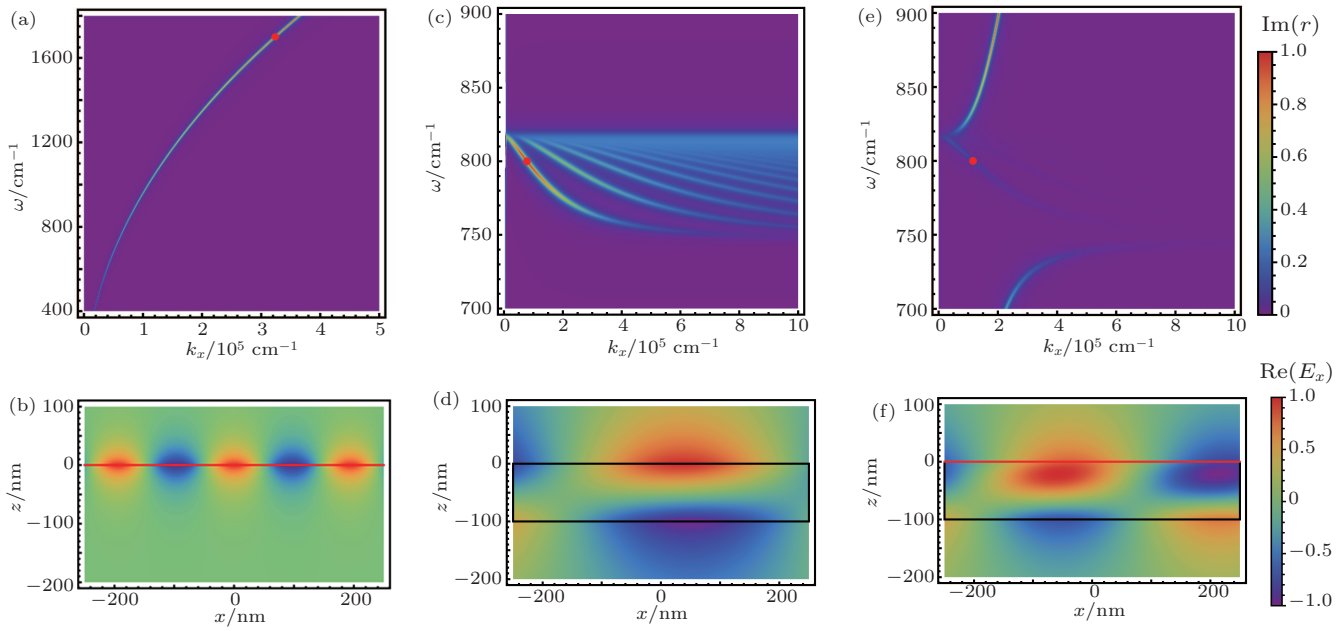


Fig. 3. (color online) Dispersions and field distributions of the modes for the free-standing graphene monolayer and the type-I band of the graphene–hBN heterostructure. The dispersions for (a) graphene ($E_\mathrm{F} = 0.5$ eV), (c) hBN and (e) their hybrid structure. (b), (d), (f). The field profiles of the modes of graphene, hBN and their hybrid structure at $\omega = 1700\ \mathrm{cm}^{-1}$, $800\ \mathrm{cm}^{-1}$, and $800\ \mathrm{cm}^{-1}$, respectively. The corresponding frequency positions in the left dispersion figures are indicated by red dots. The black lines in the field patterns profile the hyperbolic layer and the red line indicating the graphene sheet.

When covered by a graphene monolayer, as shown in Fig. 3(e), the dispersion branches of the hyperbolic film shift towards the right-hand. At $\omega = 800\ \mathrm{cm}^{-1}$, the momentum k_x of the mode changes from $6.8 \times 10^4\ \mathrm{cm}^{-1}$ to $10.2 \times 10^4\ \mathrm{cm}^{-1}$, as denoted by the red dots in Figs. 3(c) and 3(e), meaning the reduction of the plasmon wavelength $\lambda_\mathrm{p} = 2\pi/k_x$. The mode field patterns are slightly modified as shown in Figs. 3(d) and 3(f). This wavelength can be calculated through the equation describing the poles of reflection coefficient. Neglecting high orders of k_x for simplicity, one could have the change of plasmon wavelength $\Delta\lambda$ induced by graphene.[13]

$$\Delta\lambda = \frac{\lambda_{\mathrm{g,p}}}{\pi d} \frac{\varepsilon_2^x}{1 - \varepsilon_2^x \varepsilon_2^z}. \tag{9}$$

In Eq. (9), the graphene plasmon wavelength $\lambda_{\mathrm{g,p}}$ is approximately proportional to its Fermi energy and an external gate voltage may be applied to control the plasmon wavelength of the hybrid structure. But in this case, the near-field coupling between the localized modes of graphene and the hyperbolic layer is weak due to their mismatch in the field patterns, although they match in frequencies and wavenumbers. In this sense their existences effectively modify each other's dielectric background rather than direct mode coupling.

For the type-II band, as shown in Fig. 4(a), the hyperbolic layer also possesses an infinite number of waveguide modes but with positive phase velocity. As addressed above, it takes the zero order waveguide mode ($m = 0$) as the first mode. The field distributions for the first two modes at $1500\ \mathrm{cm}^{-1}$ are plotted in Figs. 4(c) and 4(g), which show nearly symmetric and asymmetrical field patterns for these two modes, respectively. For the hybrid structure, the first hBN's waveguide branch is smoothly coupled with the graphene mode (Fig. 4(b)) due to their common symmetric patterns. This trend is evidenced from the field patterns at the frequency points of $1500\ \mathrm{cm}^{-1}$ (Fig. 4(d)), $1600\ \mathrm{cm}^{-1}$ (Fig. 4(f)), and $1700\ \mathrm{cm}^{-1}$ (Fig. 4(h)), which show a mode transition from hBN's waveguide to hybrid and then graphene's SPP modes. Because graphene has a much wider SPP band, the frequency range for the hybrid mode is solely determined by the features of the hyperbolic layer. For the hybrid structure, the dispersion curve shifts towards left side compared with the pure hBN film. At $\omega = 1600\ \mathrm{cm}^{-1}$, the momentum k_x changes from $6.56 \times 10^5\ \mathrm{cm}^{-1}$ to $1.96 \times 10^5\ \mathrm{cm}^{-1}$ after introducing the top graphene sheet.

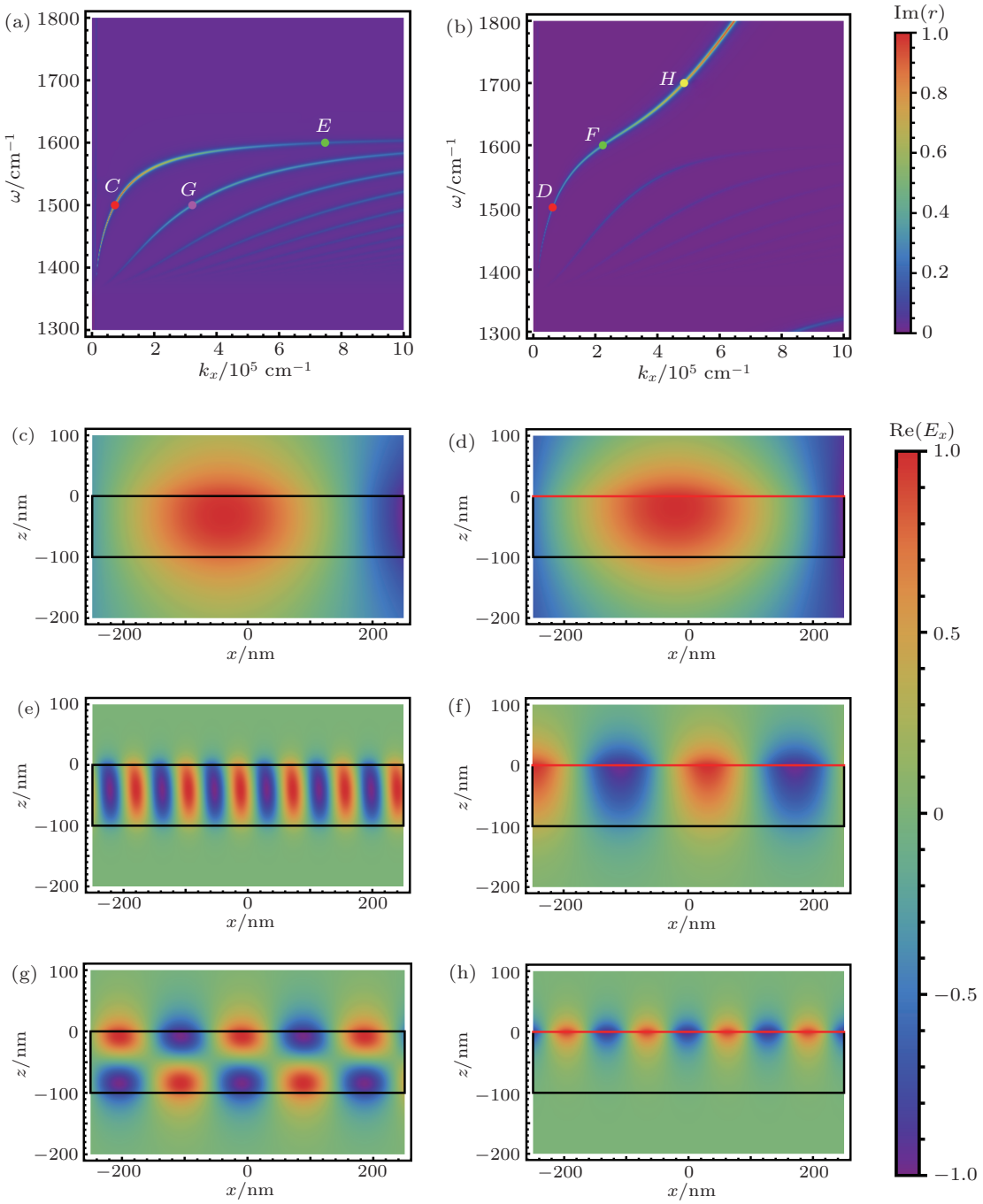


Fig. 4. (color online) Dispersions and mode patterns of the type-II band of the graphene–hBN heterostructures. The dispersion curves (a) without and (b) with graphene. The x-component electric field E_x distributions corresponding to the color points (c) C (1500 cm^{-1}), (e) E (1600 cm^{-1}), and (g) G (1500 cm^{-1}) labeled in panel (a). The E_x distributions corresponding to the color points (d) D (1500 cm^{-1}), (f) F (1600 cm^{-1}), and (h) H (1700 cm^{-1}) labeled in panel (b).

In the above, we discuss the dispersion relationship with the real momentum k_x. Generally when there exists material loss, this momentum should be a complex number with certain imaginary part κ. In the dispersion figures, the real and imaginary parts of the momentum correspond to the x-axis coordinate and the width of the bright lines, respectively.[16] Using numerical method (Lumerical Mode Solutions, with the same model and material parameters) to solve the eigenmode of the structure, we obtain the complex wavevectors at different Fermi energies for the free-standing graphene, as shown in Fig. 5(a). The loss in graphene can be controlled by increasing Fermi energy at high frequency. The real and imaginary wavevectors for a 100-nm-thick hBN film are plotted in Fig. 5(b), which shows strong loss at frequencies approaching ω_{LO}. The dispersion curves of graphene–hBN heterostructure was plotted in Fig. 5(c) at different E_{F}. With a small Fermi energy ($E_{\mathrm{F}} = 0.1$ eV), no hybrid mode exists in this band. The hybridized plasmon-phonon modes appear when E_{F} is enhanced to 0.3 eV (blue) and 0.5 eV (green). Its wavelength shifts larger by raising the Fermi energy of graphene. The wavenumber of the bounded wave is significantly reduced due to the smooth transition from hBN's lossy phonon resonance

mode to graphene's SPP mode which has a far smaller damping factor near $\omega_{\rm LO}$. It is interestingly noted that the loss factor κ is effectively suppressed when hybridization happens, in particular at frequencies near $\omega_{\rm LO}$.

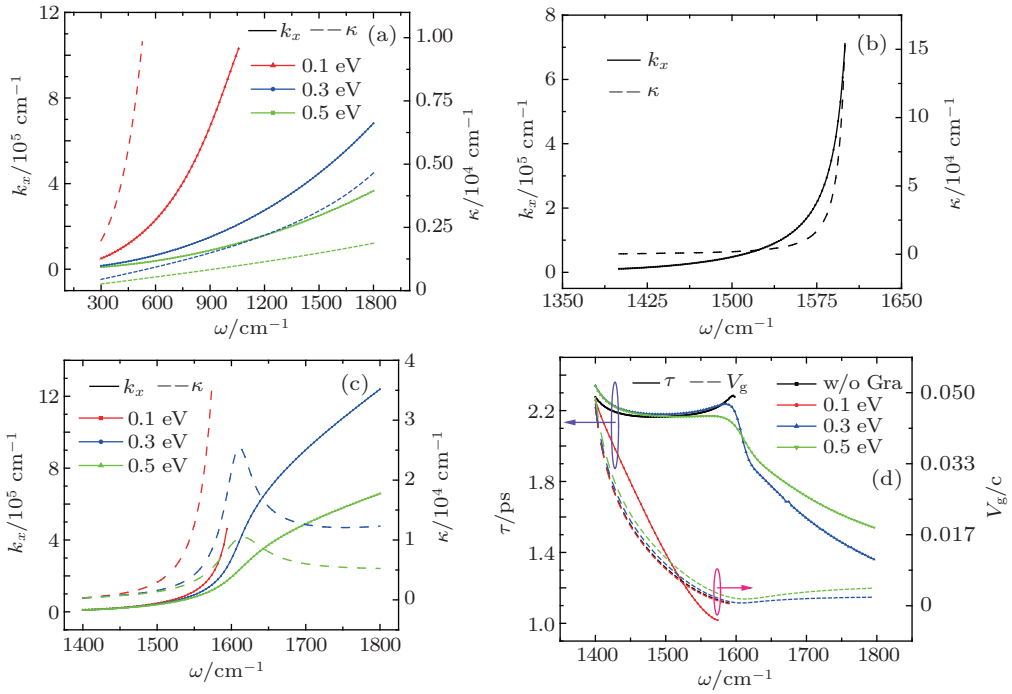


Fig. 5. (color online) Real (k_x) and imaginary (κ) part momentums of the bounded modes in graphene (a), hBN (b) and the hybrid structure (c). Three different Fermi energy levels ($E_{\rm F} = 0.1$, 0.3, 0.5 eV) for graphene have been considered. (d) The life-time τ and group velocity $V_{\rm g}$ of the hybrid polaritons at different $E_{\rm F}$. The frequency ranges in panels (b) and (d) correspond to the type-II band of hBN.

In order to characterize the polariton propagation, the propagation velocities $V_{\rm g}$ ($= {\rm d}\omega/{\rm d}k$) and the decay time of HPPs τ ($= L/V_{\rm g}$, L is the propagation length and equals $1/\kappa$) are calculated at different $E_{\rm F}$. As shown in Fig. 5(d), the velocity is about one percent of light speed in vacuum. The propagation length is about tens of micrometers (not shown in the figure) and the decay time τ is about two picoseconds which is two orders larger than the ordinary plasmons in silver.[34] Due to this significant improvement in plasmon propagation length and lifetime, the highly confined low loss graphene–hBN heterostructure is promising as a core component in nanophotonic devices.

3.2. With the AlN hyperbolic layer

AlN is a wide band gap semiconductor, and has many important applications in high-efficiency optoelectronic and laser devices. It has the similar phonon resonance features with hBN, but characterized by different equation. In the multilayer structure air/graphene/AlN/SiO_2, the dielectric function of AlN layer is described by[30]

$$\varepsilon_{h,\perp(\|)} = \varepsilon_{\infty,\perp(\|)} \frac{\omega^2_{{\rm LO},\perp(\|)} - \omega^2 - {\rm i}\omega\gamma_{{\rm LO},\perp(\|)}}{\omega_{{\rm TO},\perp(\|)} - \omega^2 - {\rm i}\omega\gamma_{{\rm TO},\perp(\|)}}. \quad (10)$$

The parameters are given in Table 1. In our architecture, the c-axis of the AlN film is assumed to be in-plane aligned, which is experimentally achievable by epitaxial growth.[35] Both of the dielectric functions are Lorentz model for phonon crystals,[36] but AlN has a slight different from the hBN. AlN only has one hyperbolic region in 610–670 cm^{-1} as shown in Fig. 6(a) (shaded orange). When the frequency increases beyond the hyperbolic region, both the in-plane and out-of-plane permittivity become negative, which is different from the hBN case.

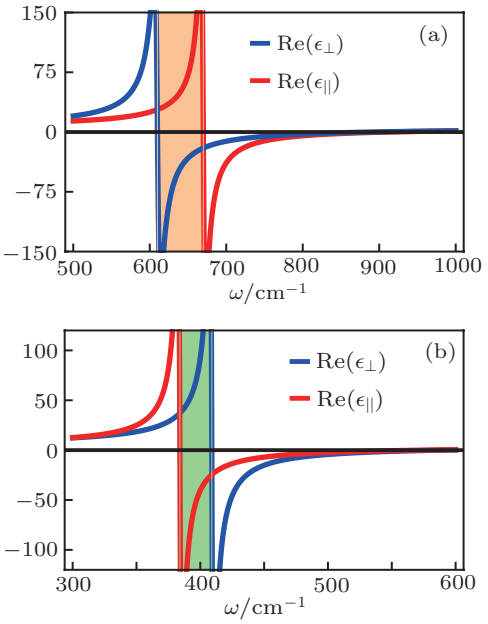


Fig. 6. (color online) Relative permittivity spectra of AlN (a) and ZnO (b). The c-axis of the crystals for AlN and ZnO is assumed to be in plane and out of plane, respectively. The dielectric functions of these two materials are described by Eq. (10). The hyperbolic regions are highlighted by the orange and green colors, respectively.

Using the same method described above, we calculate the dispersion relationship of the hybrid structure, shown in Figs. 7(a) and 7(b). The film thickness is set to be 200 nm. The damping constant of AlN is larger than hBN, which leads to relatively broader resonance line with less amplitude contrast. Here logarithmic scaling has been used for clear observing. For AlN, we observe different orders of HPP modes in the hyperbolic region (i.e., 610–670 cm^{-1}), but only the lowest zero order is strong due to the loss issue. In addition, we also observe another dispersion curve corresponding to a metallic SPP-like mode above this hyperbolic region, where AlN is fully negative in permittivity. The two bright mode lines in Fig. 7(a) have asymptotic values about 820 cm^{-1} and 855 cm^{-1} at large wavenumber, whose field patterns are plotted in Figs. 7(c) and 7(e) at 800 cm^{-1} and 880 cm^{-1}, respectively. The symmetrical waveguide and surface mode characteristics are clearly elaborated by these two figures. Here, the center of the zero order waveguide mode shifts closer to the bottom SiO_2 side due to the asymmetry of the background dielectrics. It is interesting to see that the top SPP-like mode exhibits a negative slope for frequency above 855 cm^{-1} at large wavevectors, which may be used for applications such as slow waves.[37]

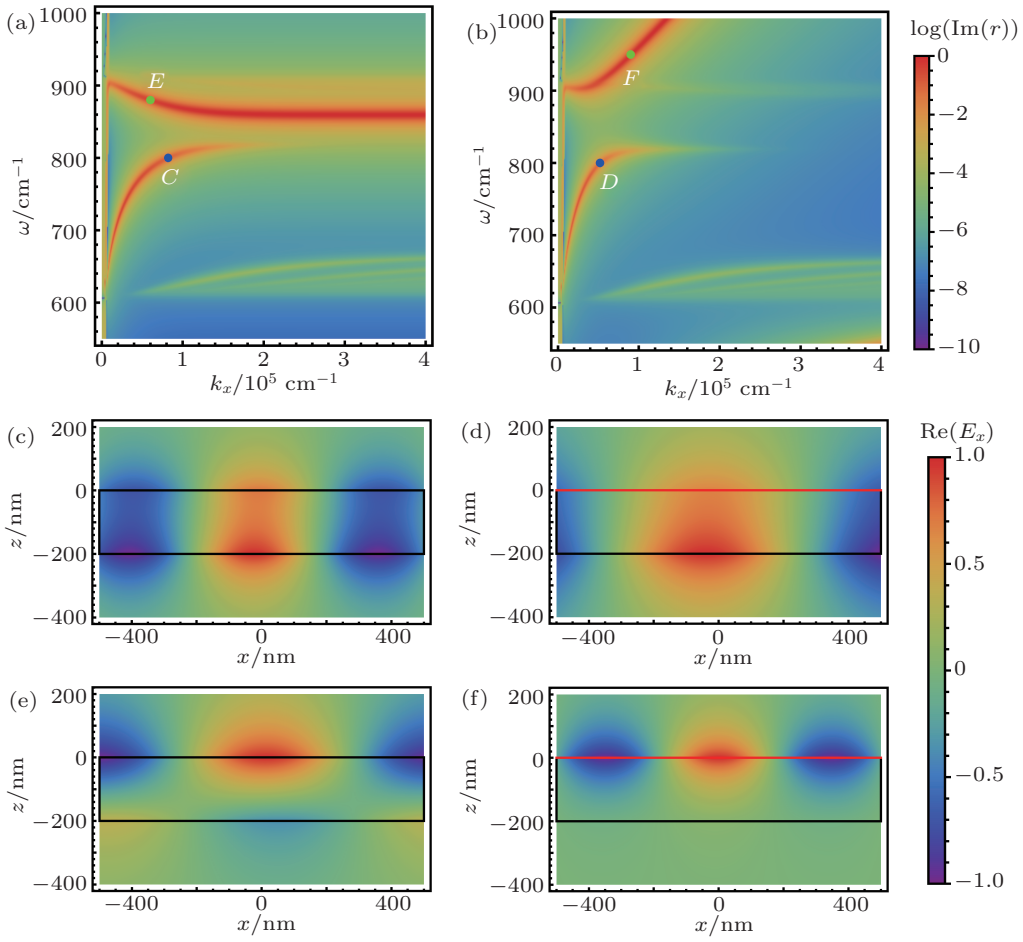


Fig. 7. (color online) Dispersions and mode patterns of the AlN and graphene-AlN. The dispersion curves (a) without and (b) with graphene. The E_x distributions corresponding to the color points (c) C (800 cm^{-1}) and (e) E (880 cm^{-1}) labeled in panel (a), and the E_x distributions corresponding to the color points (d) D (800 cm^{-1}) and (f) F (950 cm^{-1}) labeled in panel (b).

When a graphene layer is introduced on the top of the structure, both modes are modified due to their effective coupling with the SPP mode of graphene. After hybridization, the wavevector of the original lower waveguide mode is reduced. For example, the mode at 800 cm^{-1} shifts from 8.2×10^{-4} cm^{-1} to 5.2×10^{-4} cm^{-1} accompanied by a slight upward movement of the field distribution shown in Fig. 7(d). On the other side, the original SPP-like mode disappears at $\omega < 900$ cm^{-1} and a new hybrid mode above 900 cm^{-1} comes out, shown in Fig. 7(b). Figure 7(f) plots the field distribution of this hybrid mode at 950 cm^{-1}.

The influence of the material loss issues is investigated and the results are given in Figs. 8(a) and 8(b) without and with graphene, respectively. For the lower waveguide mode, the imaginary part of the mode wavevector is effectively suppressed by introducing a top graphene layer, in particular for the region near the resonance frequency ω_{LO}, where κ has a nearly ten times reduction. This result is consistent with the results described above for the graphene–hBN hybrid. This is associated with the low loss properties of graphene in this frequency range.

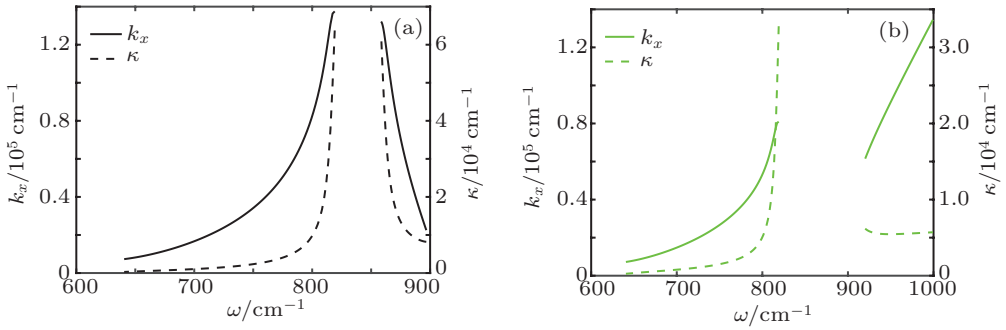


Fig. 8. (color online) Dispersion curves of graphene–AlN heterostructure with real and imaginary parts of wavevector, (a) without graphene and (b) with graphene. The Fermi energy E_F is set to be 0.5 eV.

3.3. With the ZnO hyperbolic layer

ZnO is a commonly used semiconductor sharing many properties with GaN and has been considered as a low-cost replacement to other materials for blue LEDs. Taking the free carriers and anisotropy into account, the dielectric function model of wurtzite ZnO can be expressed as the same as AlN.[31] However, we use a moderate damping constant when the single crystal ZnO is fabricated. In our calculation, the ZnO thickness is set to be 300 nm. In Figs. 9(a) and 9(b), we use a damping constant 3 to compute the dispersion curves. The band features are quite similar as those for the type-I band of the hBN film except that ZnO has a lower frequency band. Introduction of the graphene layer will change the dielectric background of the bounded modes and thus modify their dispersion. As example, it shifts from 6.8×10^4 cm^{-1} to 7.2×10^4 cm^{-1} at 400 cm^{-1}. In addition, we found that if a larger damping constant is used (e.g., $\gamma=7$), the high intensity curves become broader and the high order modes will disappear totally. The calculation shows that loss will be a key factor to influence the application of ZnO-based heterostructures. But for some specific applications such as thermal-radiation light source or thermophotovoltaic system, loss may be not a serious issue.

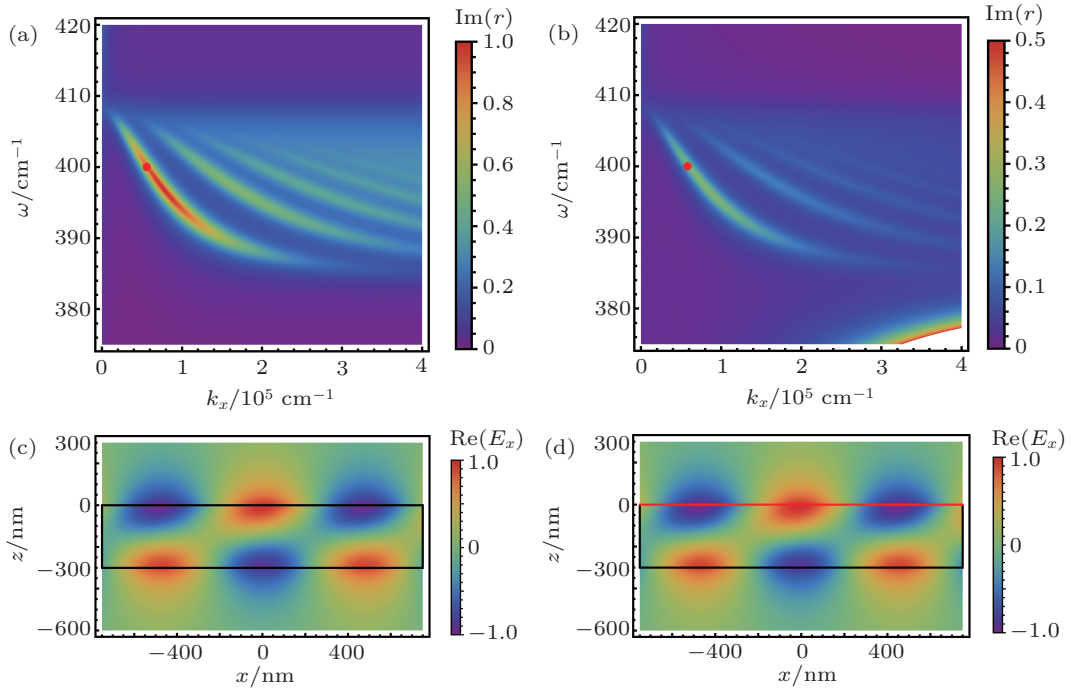


Fig. 9. (color online) Dispersions of graphene–ZnO heterostructure, (a) without graphene and (b) with graphene. (c), (d) The corresponding field profiles labeled by the red dots in panels (a) and (b) at $\omega=400$ cm^{-1}, respectively.

4. Conclusion

We have studied the features of the HPPs and SPPs in graphene covered hyperbolic materials (hBN, AlN, and ZnO) based on the dispersion spectrum. hBN has the excellent property to form highly confined plasmons with low loss. In graphene–hBN heterostructure, hybrid polaritons combining the advantages of both constituents (i.e., low loss, tunability, wide band) have been illustrated. The phonon–polartiton resonances of wurtzite AlN and wurtzite ZnO covering different infrared frequencies have their own special applications. Besides controlling the Fermi energy of graphene, the loss in these materials can be also suppressed by improving the crystallographic qualities of the crystals. But it may not be

an issue for applications such as light harvester or sensor. These hyperbolic materials supporting unique bulk waves are also useful for applications in subwavelength devices acting as spontaneous emission enhancement, super black-body thermal radiation,[38] and so on. Their electromagnetic coupling with a graphene monolayer gains more freedoms to modulate their functionalities, which is often highly desired for practical applications. Our results are meaningful for both scientific and practical purposes on the aspects of efficient subwavelength manipulation of infrared light.

References

[1] Poddubny A, Iorsh I, Belov P and Kivshar Y 2013 *Nat. Photonics* **7** 948

[2] Jacob Z 2014 *Nat. Mater.* **13** 1081

[3] Noginov M, Lapine M, Podolskiy V and Kivshar Y 2013 *Opt. Express* **21** 14895

[4] Lu D and Liu Z 2012 *Nat. Commun.* **3** 1205

[5] Kabashin A V, Evans P, Pastkovsky S, Hendren W, Wurtz G A, Atkinson R, Pollard R, Podolskiy V A and Zayats A V 2009 *Nat. Mater.* **8** 867

[6] Poddubny A N, Belov P A, Ginzburg P, Zayats A V and Kivshar Y S 2012 *Phys. Rev. B* **86** 035148

[7] High A A, Devlin R C, Dibos A, Polking M, Wild D S, Perczel J, de Leon N P, Lukin M D and Park H 2015 *Naure* **522** 192

[8] Monticone F and Al'u A 2014 *Chin. Phys. B* **23** 47809

[9] Ju L, Geng B, Horng J, Girit C, Martin M, Hao Z, Bechtel H A, Liang X, Zettl A, Shen Y R and Wang F 2011 *Nat. Nanotechnol.* **6** 630

[10] Kumar A, Low T, Fung K H, Avouris P and Fang N X 2015 *Nano Lett.* **15** 3172

[11] Woessner A, Lundeberg M B, Gao Y, Principi A, Alonso-Gonzaolez P, Carrega M, Watanabe K, Taniguchi T, Vignale G, Polini M, Hone J, Hillenbrand R and Koppens F H L 2015 *Nat. Mater.* **14** 421

[12] Caldwell J D, Vurgaftman I, Tischler J G, Glembocki O J, Owrutsky J C and Reinecke T L 2016 *Nat. Nanotechnol.* **11** 9

[13] Dai S, Ma Q, Liu M K, Andersen T, Fei Z, Goldflam M D, Wagner M, Watanabe K, Taniguchi T and Thiemens M 2015 *Nat. Nanotechnol.* **10** 682

[14] Zhang K, Zhang H and Cheng X 2016 *Chin. Phys. B* **25** 37104

[15] Dean C R, Young A F, Meric I, Lee C, Wang L, Sorgenfrei S, Watanabe K, Taniguchi T, Kim P, Shepard K L and Hone J 2010 *Nat. Nanotechnol.* **5** 722

[16] Dai S, Fei Z, Ma Q, Rodin A S, Wagner M, McLeod A S, Liu M K, Gannett W, Regan W, Watanabe K, Taniguchi T, Thiemens M, Dominguez G, Castro Neto A H, Zettl A, Keilmann F, Jarillo-Herrero P, Fogler M M and Basov D N 2014 *Science* **343** 1125

[17] Taniyasu Y, Kasu M and Makimoto T 2006 *Nature* **441** 325

[18] Lee S C, Ng S S, Al-Hardan N H, Abdullah M J, Hassan Z and Hassan H A 2011 *Thin Solid Films* **519** 3703

[19] Carrasco E, Tamagnone M, Mosig J R, Low T and Perruisseau-Carrier J 2015 *Nanotechnology* **26** 134002

[20] Wagner M, Fei Z, McLeod A S, Rodin A S, Bao W, Iwinski E G, Zhao Z, Goldflam M, Liu M, Dominguez G, Thiemens M, Fogler M M, Castro Neto A H, Lau C N, Amarie S, Keilmann F and Basov D N 2014 *Nano Lett.* **14** 894

[21] Zhan T, Shi X, Dai Y, Liu X and Zi J 2013 *J. Phys.-Condens. Mat.* **25** 215301

[22] Li Z Y and Lin L L 2003 *Phys. Rev. E* **4** 046607

[23] Xiang Y, Guo J, Dai X, Wen S and Tang D 2014 *Opt. Express* **22** 3054

[24] Zhang L, Zhang Z, Kang C, Cheng B, Chen L, Yang X, Wang J, Li W and Wang B 2014 *Opt. Express* **22** 14022

[25] Cheng H, Chen S, Yu P, Liu W, Li Z, Li J, Xie B and Tian J 2015 *Adv. Opt. Mater.* **3** 1744

[26] Messina R and Ben-Abdallah P 2013 *Sci. Rep.-UK* **3** 1383

[27] Fei Z, Andreev G O, BaoW, Zhang L M, McLeod A S, Wang C, StewartMK, Zhao Z, Dominguez G, Thiemens M, FoglerMM, TauberMJ, Castro-Neto A H, Lau C N, Keilmann F and Basov D N 2011 *Nano Lett.* **11** 4701

[28] Cai Y, Zhang L, Zeng Q, Cheng L and Xu Y 2007 *Solid State Commun.* **141** 262

[29] Dai S, Ma Q, Andersen T, Mcleod A S, Fei Z, Liu M K, Wagner M, Watanabe K, Taniguchi T, Thiemens M, Keilmann F, Jarillo-Herrero P, Fogler M M and Basov D N 2015 *Nat. Commun.* **6** 6963

[30] Ng S S, Ooi P K, Lee S C, Hassan Z and Abu Hassan H 2012 *Mater. Chem. Phys.* **134** 493

[31] Lee S C, Ng S S, Abu Hassan H, Hassan Z and Dumelow T 2014 *Thin Solid Films* **551** 114

[32] Biehs S A, Ben-Abdallah P, Rosa F S, Joulain K and Greffet J J 2011 *Opt. Express* **19** A1088

[33] Yoxall E, Schnell M, Nikitin A Y, Txoperena O, Woessner A, Lundeberg M B, Casanova F, Hueso L E, Koppens F H L and Hillenbrand R 2015 *Nat. Photonics* **9** 674

[34] Naik G V, Shalaev V M and Boltasseva A 2013 *Adv. Mater.* **25** 3264

[35] Kao H L, Shih P J and Lai C H 1999 *Jpn. J. Appl. Phys.* **38** 1526

[36] Dumelow T, Parker T J, Smith S R P and Tilley D R 1993 *Surf. Sci. Rep.* **17** 151

[37] Dionne J A, Verhagen E, Polman A and Atwater H A 2008 *Opt. Express* **16** 19001

[38] Guo Y, Newman W, Cortes C L and Jacob Z 2012 *Adv. OptoElectron.* **2012** 1